Journal of Protein Chemistry, Vol. 15, No. 2, 1996

The Nanometer-Scale Structure of Amyloid-β Visualized by Atomic Force Microscopy

W. B. Stine, Jr.,[1] S. W. Snyder,[2] U. S. Ladror,[2] W. S. Wade,[2] M. F. Miller,[1] T. J. Perun,[2] T. F. Holzman,[2,3] and G. A. Krafft[4]

Received November 3, 1995

Amyloid-β (Aβ) is the major protein component of neuritic plaques found in Alzheimer's disease. Evidence suggests that the physical aggregation state of Aβ directly influences neurotoxicity and specific cellular biochemical events. Atomic force microscopy (AFM) is used to investigate the three-dimensional structure of aggregated Aβ and characterize aggregate/fibril size, structure, and distribution. Aggregates are characterized by fibril length and packing densities. The packing densities correspond to the differential thickness of fiber aggregates along a z axis (fiber height above the x–y imaging surface). Densely packed aggregates ($\geq$100 nm thick) were observed. At the edges of these densely packed regions and in dispersed regions, three types of Aβ fibrils were observed. These were classified by fibril thickness into three size ranges: 2–3 nm thick, 4–6 nm thick, and 8–12 nm thick. Some of the two thicker classes of fibrils exhibited pronounced axial periodicity. Substructural features observed included fibril branching or annealing and a height periodicity which varied with fibril thickness. When identical samples were visualized with AFM and electron microscopy (EM) the thicker fibrils (4–6 nm and 8–12 nm thick) had similar morphology. In comparison, the densely packed regions of $\sim\geq$100 nm thickness observed by AFM were difficult to resolve by EM. The small, 2- to 3-nm-thick, fibrils were not observed by EM even though they were routinely imaged by AFM. These studies demonstrate that AFM imaging of Aβ fibrils can, for the first time, resolve nanometer-scale, z-axis, surface-height (thickness) fibril features. Concurrent x–y surface scans of fibrils reveal the surface submicrometer structure and organization of aggregated Aβ. Thus, when AFM imaging of Aβ is combined with, and correlated to, careful studies of cellular Aβ toxicity it may be possible to relate certain Aβ structural features to cellular neurotoxicity.

KEY WORDS: AFM; atomic force microscopy; amyloid beta; Alzheimer's disease; aggregation; fibril.

1. INTRODUCTION

Amyloid-β (Aβ) is a 39- to 43-amino acid peptide that comprises the major protein component of neuritic plaques and vascular deposits that appear in Alzheimer's disease (AD). Its sequence was first detemined by Glenner and Wong (1984*a, b*) and Masters *et al.* (1985) and this discovery led to the eventual identification of the gene encoding the amyloid precursor protein (βAPP) (Kang *et al.*, 1987). The exact physiological role of βAPP is still unknown, though it is clear that proteolytic processing of this transmembrane protein leads to the formation of Aβ. Aβ has been implicated as a

[1] Cellular and Microscopic Research, Abbott Laboratories, Abbott Park, Illinois 60064.
[2] Protein Biochemistry, D-46Y, AP-10-214, Discovery Research, Abbott Laboratories, Abbott Park, Illinois 60064-3500.
[3] To whom correspondence should be addressed.
[4] Department of Molecular Pharmacology and Biological Chemistry, Northwestern University, Chicago, Illinois.

0277-8033/96/0200-0193$09.50/0

causative or contributing agent in AD by virtue of neurotoxicity studies *in vitro* (Yankner *et al.*, 1989; Koo *et al.*, 1990; Pike *et al.*, 1993; Giordano *et al.*, 1994; Goodman and Mattson, 1994; Goodman *et al.*, 1994; Lambert *et al.*, 1994). In addition, cell culture studies demonstrated that several βAPP mutants that have been linked to early-onset familial AD (Goate *et al.*, 1991; Goate and Crawford, 1992; Selkoe, 1993; Golde *et al.*, 1992) generated substantially higher levels of Aβ *in vitro* (Cai *et al.*, 1993).

Experimental evidence supports the observation that Aβ specimens must be "aged" or aggregated in order to elicit neurotoxic responses. However, many laboratories have had difficulties reproducing neurotoxicity results on a consistent basis, even when specimens of Aβ have been aged according to precisely defined aggregation protocols. We and others have demonstrated that the aggregation of Aβ depends on a variety of factors and conditions (e.g., *p*H, ionic strength, peptide concentration, temperature, and mixing protocol), variations of which are likely to affect final aggregate structure in addition to aggregation kinetics (Snyder *et al.*, 1994). A wide range of analytical techniques have been employed to study aged Aβ in order to form a better understanding of how handling conditions affect aggregate structure. Circular dichroism, infrared spectroscopy, and solid-state NMR have been used to assess particular secondary structure characteristics of Aβ aggregates (Simmons *et al.*, 1994; Hilbich *et al.*, 1991, Fraser *et al.*, 1992; Spencer *et al.*, 1991; Zagorski and Barrow, 1992; Barrow *et al.*, 1992). Data from these studies suggest that Aβ aggregates exist as extended cross-β-pleated sheet assemblies.

Electron microscopy (EM) has been the primary technique employed to characterize Aβ fibril morphology. EM studies show a range of fibril diameters for synthetic and purified human specimens. The most commonly reported fibril diameters range from 5 to 12 nm (Merz *et al.*, 1983; Kirschner *et al.*, 1986; Roher *et al.*, 1986; Fraser *et al.*, 1992, 1994). EM and fiber X-ray diffraction studies suggest that the larger fibrils organize as extended chains of cross β-sheet consisting of four to six globular subunits that coalesce into a hollow rod structure (Kirschner *et al.*, 1986; Miyakawa *et al.*, 1986; Fraser *et al.*, 1991). EM has also provided evidence of 2.5 to 3.5-nm protofilaments within Aβ fibrils (Shirahama and Cohen, 1967; Merz *et al.*, 1983). However, questions remain about the effects of negative stain on fibril dimensions, and fibril substructure has been more difficult to identify in full-length Aβ 1–40 (Fraser *et al.*, 1991). With these and other issues in mind, we report the first high-resolution structural characterization and dimensional analysis of Aβ using atomic force microscopy (AFM). This method of structural analysis is distinct from conventionally applied microscopy techniques in that structure is detected without the need for stains, fixatives, exposure to vacuum, or an electron beam. We document several topographically distinct Aβ structural forms that ultimately may be correlated with particular physiological neurotoxic responses.

AFM is a unique and powerful tool for structural analysis of biological specimens because of its capability to image nonconductive specimens under a variety of conditions (for reviews see Hansma and Hoh, 1994; Yang and Shao, 1995). A significant advantage over conventional electron microscopy is its ability to image in a fluid or ambient environment (atmospheric pressure and room temperature). AFM also entails minimal sample manipulation and affords very high spatial resolution (molecular to atomic resolution under ideal conditions) in providing three-dimensional topographic information.

AFM has been used previously to study the nanometer substructure of other biological polymers, such as collagen (Baselt *et al.*, 1993; Chernoff and Chernoff, 1992), DNA (Hansma *et al.*, 1995), microtubules (Vater *et al.*, 1995), and the bacterial polysaccharide acetan (Kirby *et al.*, 1995). Substructural analysis of actin filaments using AFM has revealed features corresponding to the expected size of actin monomers (Weisenhorn *et al.*, 1990). AFM studies of two-dimensional protein arrays such as the hexagonally packed intermediate (HPI) layer (Karrasch *et al.*, 1994) and the OmpF porin surface (Schabert *et al.*, 1995) also have shown excellent correlation with previous EM and crystallographic findings. AFM analysis of gap junctions under physiologic conditions provided images of single junctions and details down to the level of the central ion pore (Hoh *et al.*, 1991, 1993). These studies demonstrate the power of AFM as an emerging tool for imaging and analyzing small biological structures.

2. MATERIALS AND METHODS

2.1. Aβ Preparation

Aβ 1–40 was synthesized, purified, and handled as described by Snyder *et al.* (1994). Previous characterization of Aβ 1–40 demonstrated that Aβ 1–40 remains monomeric in DMSO at high concentrations (6–10 mM). Starting from concentrated stock solutions in DMSO, Aβ was diluted into sterile-filtered 10 mM phosphate, 150 mM NaCl, *p*H 7.4 phosphate-buffered saline (PBS) and immediately vortexed. Peptide solutions were not agitated except for gentle inversion prior to specimen mounting. Specimens were aged in PBS at room temperature at concentrations ranging from 10 to 500 μM. No fibril degradation or indications of bacterial contamination were observed in specimens aged for up to 1 year.

2.2. Negative-Stain EM Specimen Preparation and Analysis

Specimens were prepared for EM by floating a 300 mesh carbon-Formvar grid on a 50-μl droplet of Aβ at a concentration of 50 μM for 5 min. Excess liquid was wicked off with filter paper. Specimens were then stained with 2% aqueous uranyl acetate for 5 min. Excess uranyl acetate was wicked off with filter paper and grids were allowed to dry before analysis. EM was performed using a Phillips CM12 transmission electron microscope (Phillips Electronic Instruments, Mahwah, NJ) operating at an acceleration voltage of 80 kV. Magnification was calibrated using catalase crystals (Ted Pella Inc., Redding, CA). Negatives from both Aβ and catalase specimens were scanned on a Umax Ultra Vision 1200S (Umax Data Systems, Taiwan) flatbed scanner and dimensions were measured using NIH Image v1.41 software.

2.3. AFM Specimen Preparation and Analysis

Aβ specimens were prepared for AFM analysis by spotting 10 μl of Aβ suspension (10–500 μM) on either one of two different substrates, freshly cleaved mica (Ted Pella Inc.) or pyrolytic graphite (ZYB Grade, Advanced Ceramics, Cleveland OH). Droplets were incubated on the substrate at room temperature for 5–10 min, then excess liquid was wicked off with filter paper. Two procedures were used to lower the background caused by adsorbed salts. Specimens were either briefly rinsed with distilled H_2O after mounting or were dialyzed against distilled H_2O using a 6- to 8-kD cutoff membrane for 2 hr at room temperature prior to mounting. Specimens were also imaged without rinsing or dialysis and no detectable difference in aggregate or fibril structure was observed.

Image data were generated on a NanoScope III MultiMode scanning probe workstation (Digital Instruments, Santa Barbara CA), using either a "J"-type scanner with *xy* range 150 μm or an "E"-type scanner with *xy* range of 15 μm. Two different imaging modes were employed. Contact mode imaging was performed using the glass fluid cell filled with 0.2-μm-filtered isopropanol. Isopropanol has been shown to improve image quality (Hansma *et al.*, 1992), probably by eliminating meniscus forces between the AFM tip and sample. The probes used for contact mode imaging were either oxide-sharpened silicon nitride NP-S Nanoprobes (Digital Instruments) with nominal spring constants of 0.06–0.58 kN/m or silicon Ultralevers (Park Scientific, Sunnyvale CA) with nominal spring constants of 0.16 kN/m. The second imaging mode, TappingMode™ (Digital Instruments), was performed under ambient conditions (23°C, 25% relative humidity) using etched silicon TESP Nanoprobes (Digital Instruments). For most samples, contact force was minimized by adjusting the set point to a level just above the point where the tip began to pull off the surface. The AFM maps a sample surface, collecting three-dimensional information and storing a predetermined number of *x, y, z* coordinates in a data set. In these figures a 512 × 512 point data set was collected and plotted in *x, y,* and *z*. Thickness information is represented by contrast, with light areas being taller than dark. The *z*-scale magnitude that determines image contrast is arbitrarily set to provide the best image representation and varies from image to image.

3. RESULTS AND DISCUSSION

3.1. Aggregate and Fibril Morphology

At relatively low magnifications (10,000–50,000 × mag), many morphological features of the Aβ aggregates appeared similar when analyzed by AFM and EM. Densely packed regions made up of elongated fibrils were commonly observed in aged Aβ specimens by AFM (Fig. 1). By EM, these

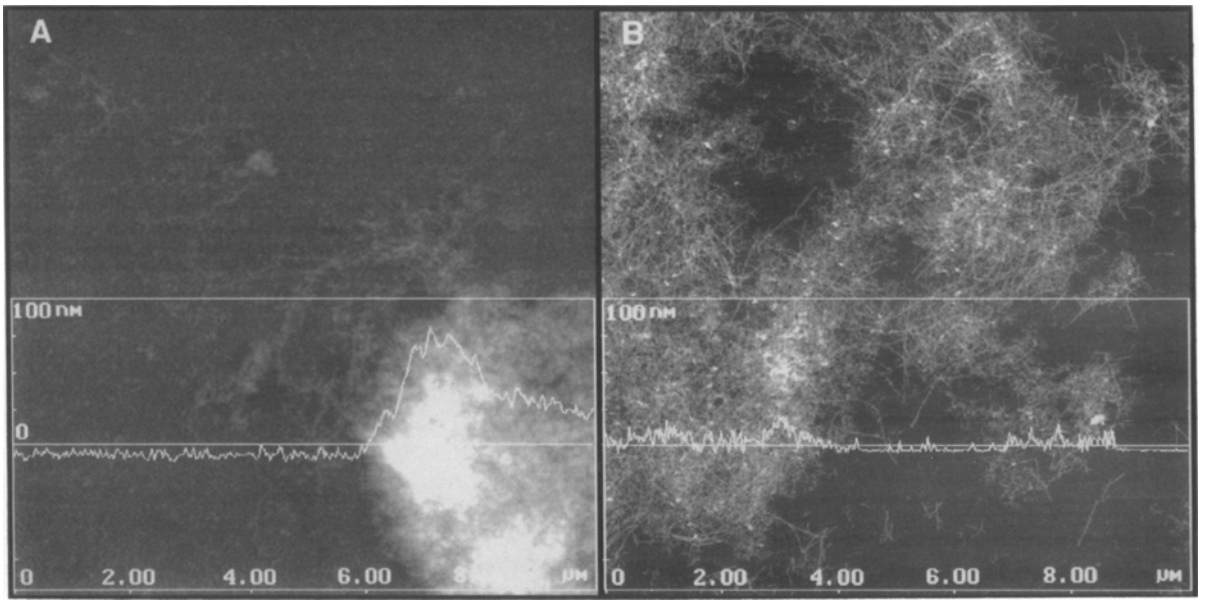

Fig. 1. Two different aggregrate formations of Aβ displayed as top-view plots superimposed with a cross-section plot. The figure images are each 10 μm square. A densely packed aggregate of Aβ situated in the lower right corner of (A) measures up to 100 nm, whereas the more diffuse aggregate in (B) has no regions greater than 50 nm above the sample substrate. The position of the centerline in each cross-section plot corresponds to the location on the image where the plot data was sampled. Thickness information in these images is represented by contrast difference, with thicker objects appearing lighter. (A) Specimen: 50 μM Aβ 1–40 aged for 7 weeks in sterile, high-salt PBS (500 mM NaCl, 10 mM PO_4, *p*H 7.4). Aβ peptide aggregates remained adherent to the mica even after multiple rinsing steps (data not shown); however, specimens were routinely rinsed only once (B) Specimen: Aβ 1–40 aged for 50 weeks in PBS, then dialyzed against distilled H_2O for 2 hr. Specimens in both (A) and (B) were imaged in contact mode under isopropanol.

densely packed regions appeared as dark patches with little to no fibril resolution (data not shown). One of the first differences observed with AFM that was not apparent by EM was the variation in aggregate thickness. The Aβ aggregate in Fig. 1A measures up to 100 nm thick, whereas the aggregate in Fig. 1B measures less than 50 nm. Aggregate density may be measured to some extent using EM by counting the number of fibrils or the number of fibril crossovers in a given field, although it is difficult for the electron beam to penetrate more densely packed amyloid structures. The majority of EM images in our work (Fig. 2) (also see Snyder *et al.*, 1994) and in previous published reports (e.g., Fraser *et al.*, 1992, 1994) portray Aβ aggregates as fields of dispersed fibrils, often appearing no more than two or three fibrils deep. In contrast, AFM reveals that identical samples appear to contain many densely aggregated regions measuring 50–1000 nm thick (data not shown). AFM analysis can differentiate between dispersed and densely packed Aβ aggregates by measuring the thickness of the aggregate on the imaging surface (Fig. 1). Although both aggregate structures in Fig. 1 were made up of elongated fibrils of chemically identical peptide, they appear to condense to different extents depending on aggregation conditions and lengths of incubation.

3.2. AFM Measurements and Comparison to EM Data

Fibril thickness values (4–9 nm) measured by AFM are in good agreement with the most frequent fibril diameters (7–12 nm) determined by EM analysis for both synthetic and purified human Aβ 1–40 (Fraser *et al.*, 1991; Merz *et al.*, 1983; Roher *et al.*, 1986). AFM measurement of fibril thickness can be influenced by two inherent distortions. The widths of features that are close in size to the radius of curvature of the AFM tip tend to be exaggerated by convolution, while the thickness of deformable biomolecules is often underestimated due to sample compression. Figure 3 presents a diagram of these phenomena to illustrate the differences between measured and estimated dimensions. In spite of the

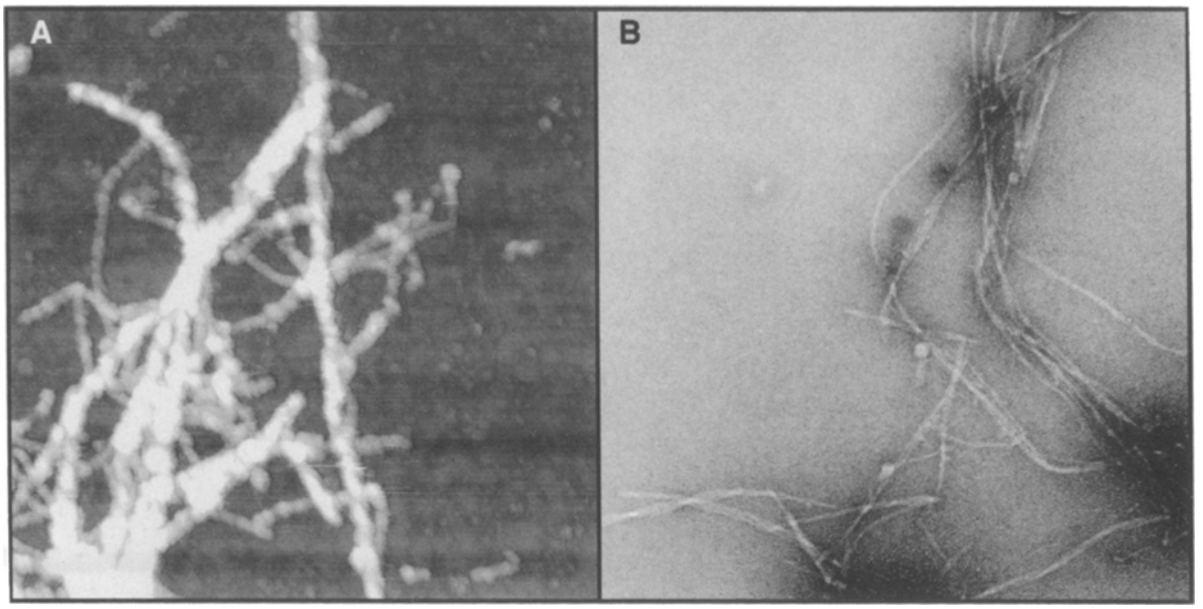

Fig. 2. Comparison of negative-stain EM and AFM images of morphologically similar regions of the same Aβ specimen (50 μM Aβ 1–40 aged for 42 weeks in sterile PBS at 23°C). The figure images are each 1 μm square. (A) Fibrils 6–8 nm tall with some larger bundles. (B) In the AFM image fibril widths appear much larger due to tip convolution. Negative-stain EM of the same specimen revealed fibrils 8–12 nm wide. Larger bundles of fibrils and dense aggregates were also present in the specimen prepared for AFM; however the majority of Aβ fibrils appeared more loosely associated by EM.

discrepancies between the measured and actual sizes, the distortion effects are reasonably predictable and consistent.

As an additional calibration aid, simultaneous imaging of double-stranded plasmid DNA molecules and Aβ aggregates was carried out to assess imaging resolution and the extent of distortion induced by the AFM tip (Fig. 4). The observed dimensions and image quality of DNA molecules

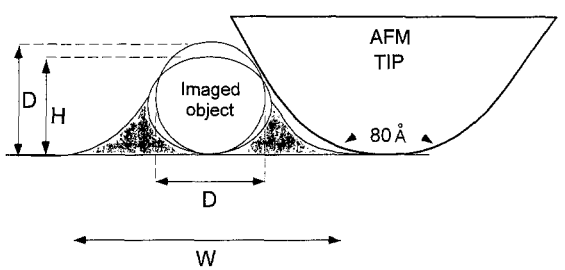

Fig. 3. Model showing the effects of sample compression and tip convolution on deformable biomolecules. *D*, Actual diameter of a cylindrical sample; *H*, the measured thickness, which is smaller than the actual thickness due to sample compression; *W*, the measured width, which is larger than the actual width primarily due to convolution that is proportional to the end radius of curvature of the tip. Sample compression may also contribute to the increased measured widths of biomolecules.

are very sensitive to tip geometry and imaging conditions. Thickness measurements on the plasmid DNA ranged from 1.0 to 1.6 nm, varying only 0.4–0.6 nm along the length of the molecule. This value is 0.6–0.4 nm less than the diameter of double-strand DNA reported by X-ray crystallography (Dickerson *et al.*, 1982). The discrepancy between these values is most likely due to sample compression, although piezo nonlinearity, feedback loop response, and frictional effects may contribute to a lesser extent (Hoh *et al.*, 1993).

Most of the Aβ fibrils observed by AFM were typically 3–5 times the measured thickness of coabsorbed DNA. Therefore, by AFM we estimate that Aβ fibrils range from 6 to 10 nm thick. the plot in Fig. 4 traces a cross-sectional region that includes an open circular plasmid molecule situated above the edge of a larger Aβ aggregate. Two points on the plasmid molecule measure 1.5 nm thick, whereas the end of an Aβ fibril protruding from an aggregate measures 5 nm. Measurements of fibril width from negative-stain EM images of the same Aβ sample (Fig. 2) yielded a fibril thickness of 8–12 nm. Taking into account variation in thickness along the fibril axis, the AFM and EM estimations are in close agreement.

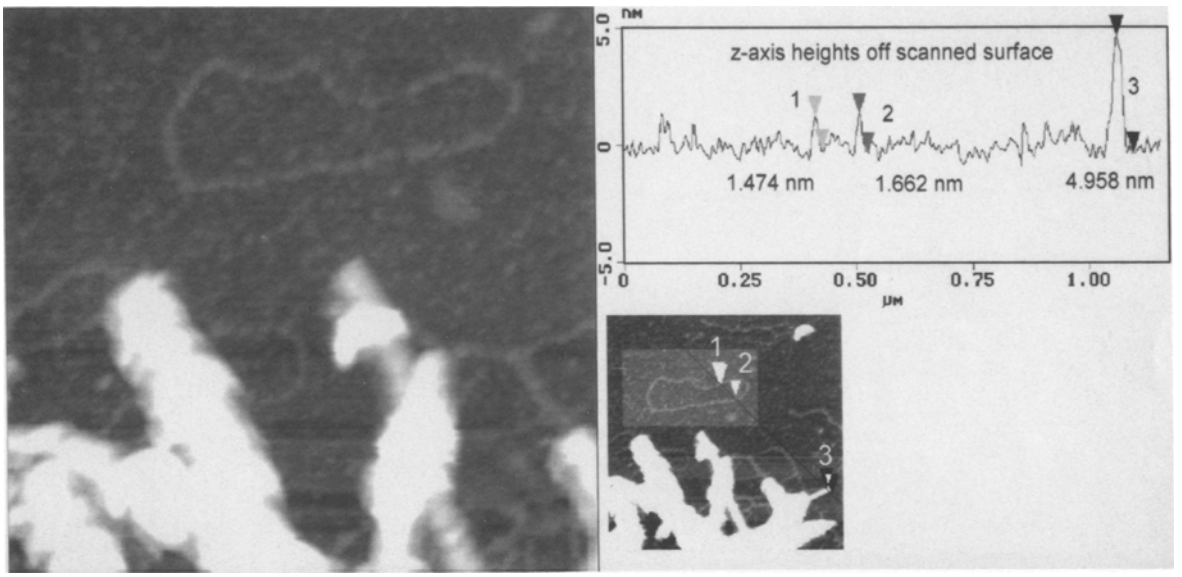

Fig. 4. Section analysis of Aβ coimaged with pUC18 DNA. The figure images are each 740 nm square. The measured thickness of the plasmid is approximately 1.5 nm above the substrate surface. One of the fibrils protruding from the aggregate measures approximately 5 nm above the substrate. This Aβ aggregate is comprised of densely packed shorter fibrils. Most of the Aβ aggregate thickness information is intentionally presented out of range to provide enough contrast to visualize the plasmid DNA. Plasmid DNA (10 μg/ml) was spotted on the mica substrate, dried, and rinsed with distilled H_2O. The Aβ 1–40 (50 μM, 3 weeks in PBS) was spotted on top of the mounted DNA, and the sample was imaged in contact mode under isopropanol using silicon Ultralever tips.

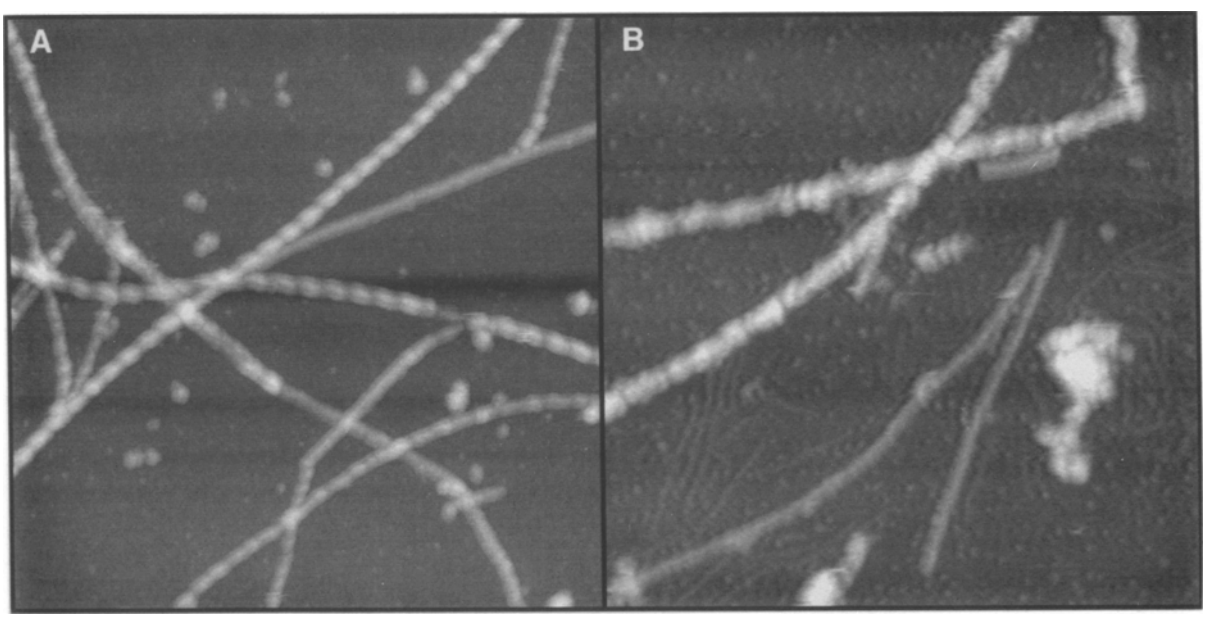

Fig. 5. Both periodic and smooth fibrils (250 μM Aβ 1–40 aged 3 weeks; imaged in contact mode under isopropanol). Image size is (A) 1 μm square, (B) 584 nm square. The fibrils situated in the lower portion of (A) and the upper region of (B) are estimated to be 8 nm thick with poorly resolved periodicity along the fibril axis, whereas the slightly thicker fibrils in (A) (estimated to be 12 nm thick) have a more pronounced repeat structure. Branching can also be observed between periodic–periodic (left) and smooth–periodic (upper right) fibrils. The thicker fibrils in (B) have similar dimensions and structure to the fibrils in the lower third of (B) (~8 nm thick), whereas the thicker periodic fibrils in (B) are estimated to be ~12 nm thick. Three different fibril structures are present in (B). Two thick fibrils (estimated to be 8–12 nm thick) with poorly resolved periodicity are present in the upper half of the image. In the lower half of the image, two intermediate fibrils (estimated to be 4–6 nm thick) appear smooth or featureless. Very small filaments (estimated to be 2–3 nm thick) can be observed between the thicker fibrils.

3.3. Fibril Substructure

Another striking feature of Aβ revealed by AFM was the distinct axial periodicity observed in some specimens (Figs 5 and 6). Fibrils 8–12 nm thick were observed with a pronounced axial periodicity of 25 nm. Smooth or featureless fibrils of the same dimensions were also present in this specimen. The 25 nm peak-to-peak spacing for the periodic fibrils appeared to vary with fibril

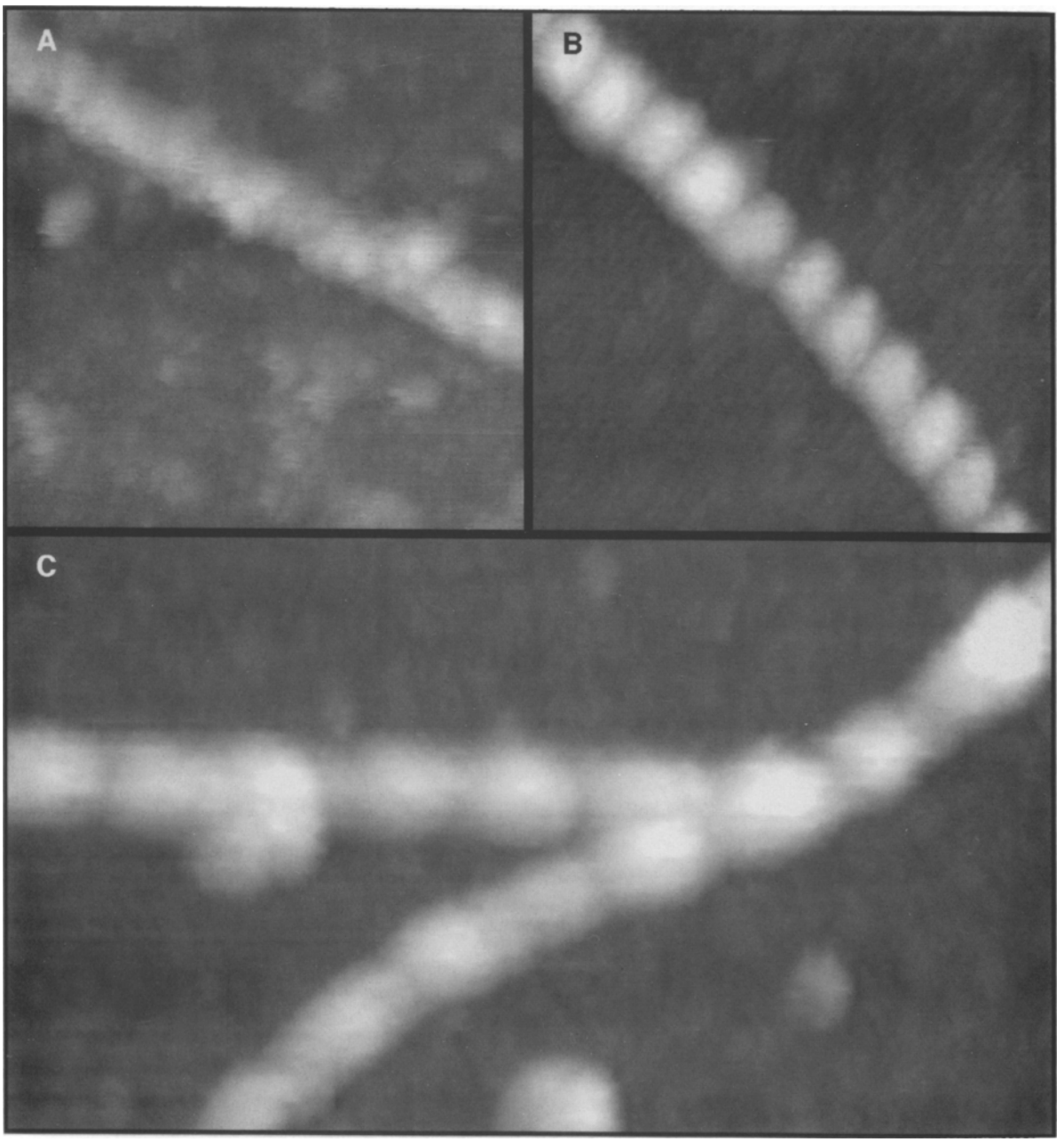

Fig. 6. Three fibril structures at high resolution can be observed for Aβ (250 μM Aβ 1–40 aged 3 weeks in PBS, dialyzed, and imaged using contact mode in isopropanol). Figure image size is (A, B) 1 μm square, (C) 350 × 175 nm. The fibril in (A) is estimated to be 8–10 nm thick and has no detectable periodic structure. The fibril in (B) has distinct axial periodicity but the same thickness (8–10 nm). Peak-to-peak spacing along the axis fibril is ~25 nm. (C) An example of a branched periodic-to-periodic fibril branch point. The estimated thickness (8–10 nm) for (C) is the same as for (A) and (B). An interesting feature of the branch point is that there is no significant increase in fibril thickness where the two fibrils intersect. This might indicate that some fibril branch points arise from a fibril growing out of an existing structure.

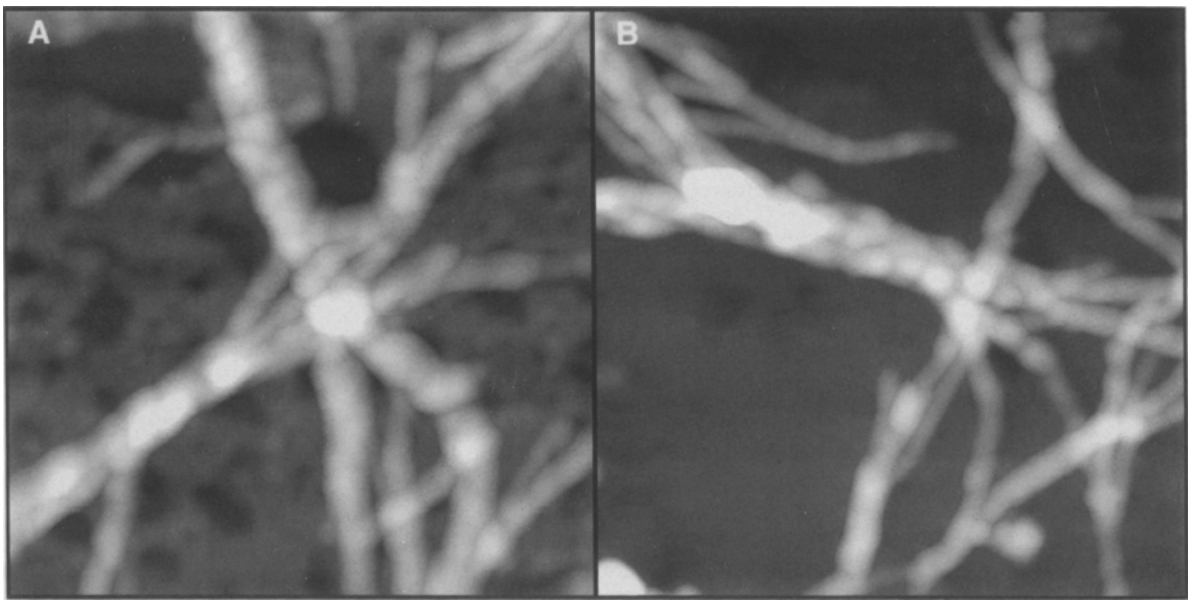

Fig. 7. Two examples of fibril assemblies where smaller fibrils intertwine to form larger fibril bundles (50 μM Aβ 1–40, 50 weeks in PBS, then dialyzed against distilled water, mounted on HOPG, and imaged in TappingMode). Figure image size is (A) 625 nm square, (B) 1 μm square. A patchy film about 2–3 nm thick of what is thought to be small globular aggregates of Aβ covers most of the substrate in (A). The bundle in (B) has a more nodular, rather than twisted surface structure. At this time we are unsure as to the conditions that promote the formation of nodular bundles as opposed to fibrils.

thickness. Thicker fibrils tended to have longer periods and a better defined axial repeat. Additional substructural features observed using AFM included fibril branch points. Both periodic and smooth fibrils often formed branches. These junctions could exist between periodic–periodic fibrils (Fig. 6C) and smooth–periodic fibrils (Fig. 5A, upper right). In some cases there was no apparent increase in fibril thickness (Fig. 6C). However, in others the branched fibrils are clearly emanating from a larger bundle (Fig. 7).

3.4. Unique Aβ Populations as Measured by Fibril Thickness

AFM indicates Aβ fibrils may be grouped into three size classes (Fig. 8). The large fibrils range from 8 to 12 nm thick, intermediate fibrils from 4 to 6 nm thick, and a unique population of very small fibrils was estimated to be 2–3 nm thick. All three populations of Aβ fibrils are imaged simultaneously in Fig. 5B: an 8-nm-thick periodic fibril, two 6-nm-thick smooth fibrils, and a population of considerably thinner fibrils (estimated to be 2–3 nm thick). We have observed each of these three size classes in a variety of Aβ samples by AFM; however, the 8- to 12-nm-thick fibrils are most commonly observed. Figure 9 shows imaged samples with high densities of the thin fibrils (2–3 nm thick). Longitudinal cross-sectional averages for the thin fibrils are presented in Fig. 10. A range of fibril lengths was observed for this class of fibrils—from a few nanometers to over 500 nm.

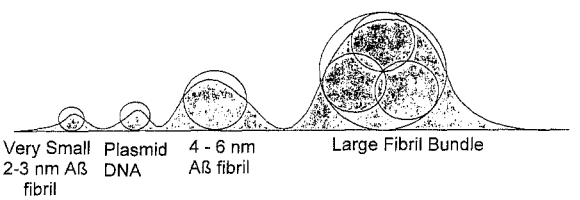

Fig. 8. A diagrammatic model of the cross section of idealized molecules showing the path that an AFM probe traces. Each of the structures will be affected by tip convolution and compression; however, the larger structures are proportionately less affected by these disturbances. Since AFM tip interactions with DNA may differ with Aβ, convolution and compression effects calibrated with DNA may not be proportional with Aβ. Therefore, we present size estimations as ranges. Evidence from EM studies indicates that larger fibrils, and possibly the 4- to 6-nm structures, are assemblies of smaller protofilaments. We observed 4- to 6-nm fibrils branching off thicker fibril assemblies and also branching in the 8- to 12-nm fibrils. However, 2- to 3-nm fibrils were only detected as isolated structures of varying length and were never observed branching off larger structures.

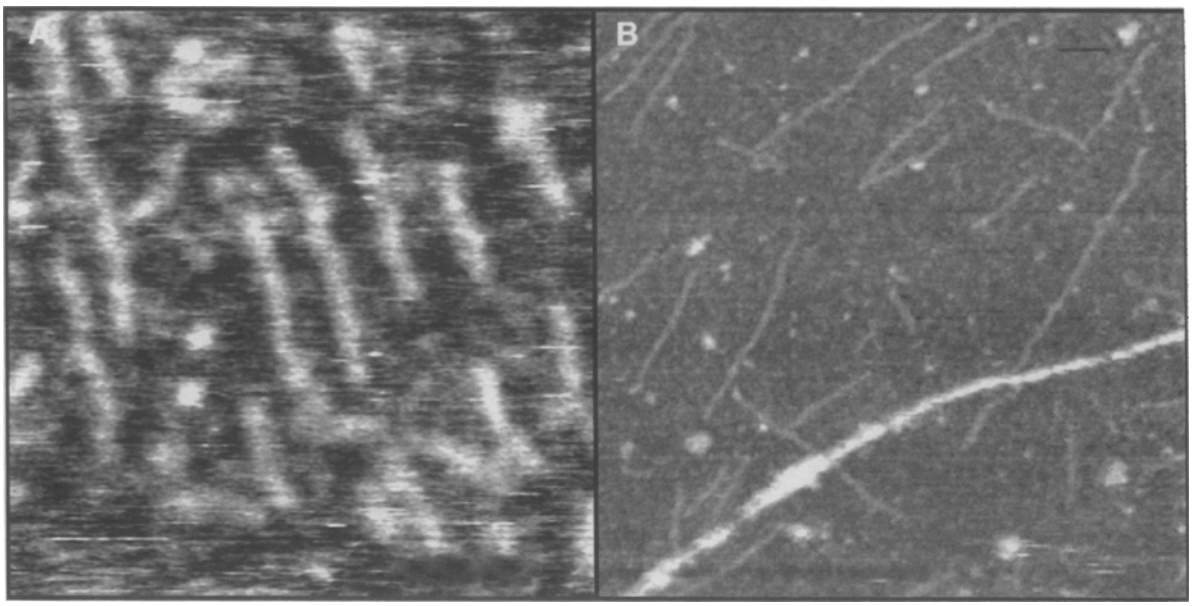

Fig. 9. AFM images from two different Aβ specimens showing the presence of very small fibrils. The figure image size is (A) 151 nm square, (B) 500 nm square. (A) Image acquired using an Aβ 1–40 specimen at 250 μM in PBS and aged 1 week. These fibrils are 2–3 nm thick, but are shorter in length. (B) Image of 250 μM Aβ 1–40, aged 10 weeks in PBS, shows a larger 4- to 6-nm fibril and a polydisperse field of smaller structures that are 2–3 nm thick.

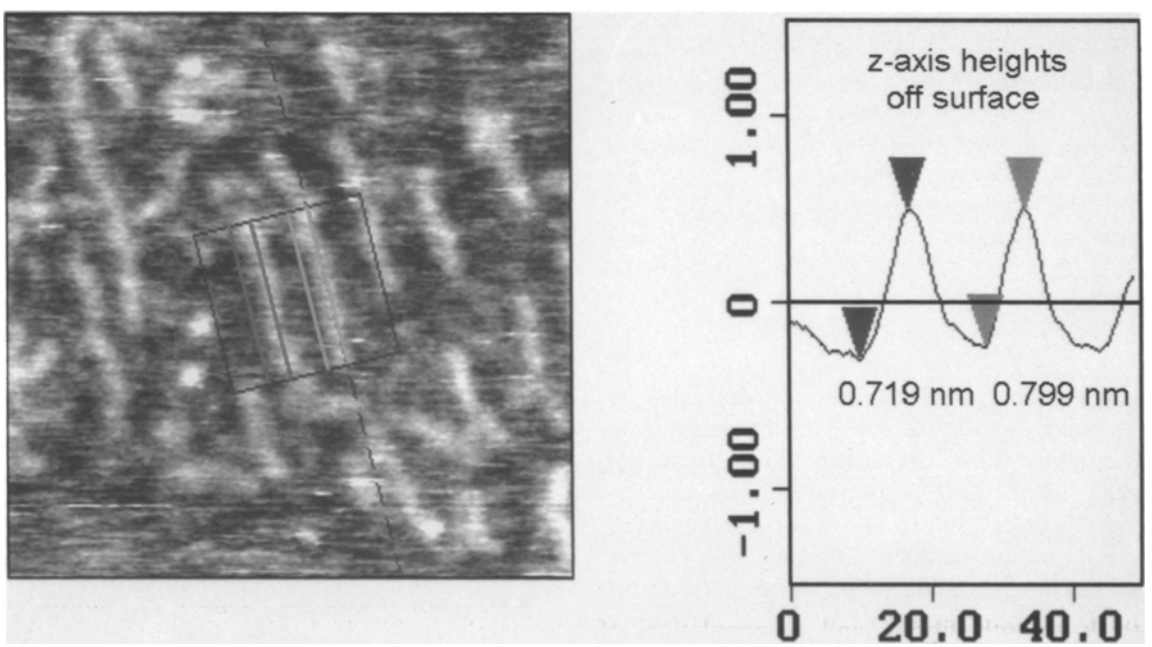

Fig. 10. Representative axial cross-section analysis of two very small Aβ fibrils from Fig. 9A. The figure image is 151 nm square. The axial cross-sectional plot represents an average thickness value along the long axis of the fibrils for the area within the box. The measured thickness of these fibrils averages from 0.7 to 1.6 nm and we estimate the actual thickness, taking into account sample compression, to be 2–3 nm.

These small fibrils have not been observed in DMSO–PBS controls nor in aged 40-amino acid peptide controls with a scrambled Aβ 1–40 sequence (data not shown). Fibrils which are 2–3 nm thick could represent either building blocks for larger fibrils or unique structures that function as kinetic traps for Aβ during the aggregation process. The only reported 2- to 3-nm structures detected by EM appear to be protofilament subunits seen in cross section (Fraser *et al.*, 1991; Miyakawa *et al.*, 1986). Fibril X-ray diffraction studies suggest that mature Aβ fibrils organize as a cross-β sheet (Kirschner *et al.*, 1986; Fraser *et al.*, 1994; Inouye *et al.*, 1993). However, a 2- to 3-nm fibril is smaller than the minimum fibril size (4–6 nm) predicted by this model. The peptide organization required to form a cross-β-sheet perpendicular to the fiber long axis within these 2- to 3-nm fibrils would need to include 4–5 β-turns to fit within a 2-nm-thick structure. It is possible that these fibrils were not detected in the fiber X-ray diffraction studies because either they represent a small fraction of the total fibril population or they do not orient (as required for diffraction) under the same conditions used for the larger fibrils.

We observe the 2- to 3-nm fibrils under a variety of conditions (ionic strength, Aβ concentration, age, etc.), even in samples that were aged for several months. However, no evidence exists for interactions between the small, 2- to 3-nm fibrils and other small fibrils to form larger fibrils or with larger 4- to 6-nm fibrils. Therefore, it is possible that these 2- to 3-nm fibrils represent a unique molecular organization of Aβ.

4. CONCLUSIONS

We have demonstrated that AFM is able to detect a wide distribution of Aβ structures from multimicrometer-thick aggregates down to nanometer-thick fibrils. AFM represents a new analytical tool that can be used to follow the course of Aβ aggregation under ambient or near-physiologic conditions. Thus it should help define mechanisms of Aβ aggregation and the influence of other neuritic plaque components such as apo E or apo J on the aggregation process. AFM also reveals a high level of topographic detail, including fibril–fibril interactions, bundle formation, and fibril branching. As a technique capable of distinguishing and characterizing structural forms of Aβ with a minimum of sample manipulation, AFM may help correlate specific aggregate structures with particular biological responses and aid in studies which may reveal the nature of neurodegenerative Aβ–cellular interactions.

ACKNOWLEDGMENTS

This work was supported in part by NIH-NIA grant AG10481. We thank Jan Hoh and Helen Hansma for review of the manuscript and Digital Instruments for equipment support.

REFERENCES

Barrow, C. J., Yasuda, A., Kenny, P. T. M., and Zagorski, M. G. (1992). *J. Mol. Biol.* **225,** 1075–1093.

Baselt, D. R., Revel, J. P., and Baldeschwieler, J. D. (1993). *Biophys. J.* **65,** 2644–2645.

Cai, X. D., Golde, T. E., and Younkin, S. G. (1993). *Science* **259,** 514–516.

Chernoff, E. A. G., and Chernoff, D. A. (1992). *J. Vac. Sci. Technol. A* **10,** 596–599.

Dickerson, R. E., Drew, H. R., Conner, B. N., Wing, R. M., Fratini, A. V., and Kopka, M. L. (1982). *Science* **216,** 475–485.

Fraser, P. E., Nguyen, J. T., Surewicz, W. K., and Kirschner, D. A. (1991). *Biophys. J.* **60,** 1190–1201.

Fraser, P. E., Nguyen, J. T., Inouye, H., Surewicz, W. K., Selkoe, D. J., Podlisny, M. B., and Kirschner, D. A. (1992). *Biochemistry* **31,** 10716–10723.

Fraser, P. E., McLachlan, D. R., Surewicz, W. K., Mizzen, C. A., Snow, A. D., Nguyen, J. T., and Kirschner, D. A. (1994). *J. Mol. Biol.* **244,** 64–73.

Giordano, T., Pan, J. B., Monteggia, L. M., Holzman, T. F., Snyder, S. W., Krafft, G. A., Ghanbari, H., and Kowall, N. W. (1994). *Exp. Neurol.* **125,** 175–182.

Glenner, G. G., and Wong, C. W. (1984*a*). *Biochem. Biophys. Res. Commun.* **120,** 885–890.

Glenner, G. G., and Wong, C. W. (1984*b*). *Biochem. Biophys. Res. Commun.* **122,** 1131–1135.

Goate, A. M., and Crawford, F. (1992). *BioEssays* **14,** 727–734.

Goate, A. M., Chartier-Harlin, M., Mullan, M. J., Brown, J., Crawford, F., Fidani, L., Giuffra, L., Haynes, A. R., Irving, N., James, L. A., Mant, R., Newton, P., Rooke, K., Roques, P., Talbot, C., Pericak-Vance, M. A., Roses, A. D., Williamson, R., Rossor, M. N., Owen, M. J., and Hardy, J. (1991). *Nature* **349,** 704–706.

Golde, T. E., Estus, S., Younkin, L. H., Selkoe, D. J., and Younkin, S. G. (1992). *Science* **255,** 728–730.

Goodman, Y. D., and Mattson, M. P. (1994). *Brian Res.* **650,** 170–174.

Goodman, Y. D., Steiner, M. R., Steiner, S. M., and Mattson, M. P. (1994). *Brain Res.* **654,** 171–176.

Hansma, H. G., and Hoh, J. H. (1994). *Annu. Rev. Biophys. Biomol. Struct.* **23,** 115–139.

Hansma, H. G., Vesenka, J., Siegerist, C., Kelderman, G., Morrett, H., Sinsheimer, R. L., Elings, V., Bustamante, C., and Hansma, P. K. (1992). *Science* **256,** 1180–1184.

Hansma, H. G., Laney, D. L., Bezanilla, M., Sinsheimer, R. L., and Hansma, P. K. (1995). *Biophys. J.* **68,** 1672–1677.
Hilbich, C., Kisters-Woike, B., Reed, J., Masters, C. L., and Beyreuther, K. (1991). *J. Mol. Biol.* **218,** 149–163.
Hoh, J. H., Lal, R., John, S. A., Revel, J. P., and Arnsdorf, M. F. (1991). *Science* **253,** 1405–1408.
Hoh, J. H., Sosinsky, G., Revel, J. P., and Hansma, P. K. (1993). *Biophys. J.* **66,** 1–15.
Inouye, H., Fraser, P. E., and Kirschner, D. A. (1993). *Biophys. J.* **64,** 502–519.
Kang, J., Lemaire, H., Unterbeck, A., Salbaum, J. M., Masters, C. L., Grzeschik, K. H., Multhaup, G., Beyreuther, K., and Muller-Hill, B. (1987). *Nature* **325,** 733–736.
Karrasch, S., Hegerl, R., Hoh, J., Baumeister, W., and Engel, A. (1994). *Proc. Natl. Acad. Sci. USA* **91,** 836–838.
Kirby, A. R., Gunning, A. P., Morris, V. J., and Ridout, M. J. (1995). *Biophys. J.* **68,** 360–363.
Kischner, D. A., Abraham, C. R., and Selkoe, D. J. (1986). *Proc. Natl. Acad. Sci. USA* **86,** 503–507.
Koo, E. H., Sisodia, S. S., Cork, L. C., Unterbeck, A., Bayney, R. M., and Price, D. L. (1990). *Neuron* **2,** 97–104.
Lambert, M. P., Stevens, G., Sabo, S., Barber, K., Wang, G., Wade, W., Krafft, G., Snyder, S., Holzman, T. F., and Klein, W. L. (1994). *J. Neurosci. Res.* **39,** 377–385.
Masters, C. L., Simms, G., Weinman, N. A., Multhaup, G., McDonald, B. L., and Beyreuther, K. (1985). *Proc. Natl. Acad. Sci. USA* **82,** 4245–4249.
Merz, P. A., Wisniewski, H. M., Somerville, R. A., Bobin, S. A., Masters, C. L., and Iqbal, K. (1983). *Acta Neuropathol.* **60,** 113–124.
Miyakawa, T., Watanabe, K., and Katsuragi, S. (1986). *Virchows Arch. B-Cell Pathol.* **52,** 99–106.
Pike, C. J., Burdick, D., Walencewicz, A. J., Glabe, C. G., and Cotman, C. W. (1993). *J. Neurosci.* **13,** 1676–1687.
Roher, A., Wolfe, D., Palutke, M., and KuKuruga, D. (1986). *Proc. Natl. Acad. Sci. USA* **83,** 2662-2666.
Schabert, F. A., Henn, C., and Engel, A. (1995). *Science* **268,** 91–94.
Selkoe, D. J. (1993). *Trends Neurosci.* **16,** 403–409.
Shirahama, T., and Cohen, A. S. (1967). *J. Cell. Biol.* **33,** 679–708.
Simmons, L. K., May, P. C., Tomaselli, K. J., Rydel, R. E., Fuson, K. S., Brigham, E. F., Wright, S., Lieberburg, I., Becker, G. W., Brems, D. N., and Li, W. Y. (1994). *Mol. Pharmacol.* **45,** 373–379.
Snyder, S. W., Ladror, U. S., Wade, W. S., Wang, G. T., Barett, L. W., Matayoshi, E. D., Huffaker, H. J., Krafft, G. A., and Holzman, T. F. (1994). *Biophys. J.* **67,** 1216–1228.
Spencer, R. G. S., Halverson, K. J., Auger, M., McDermott, A. E., Griffin, R. G., and Lansbury, P. T. (1991). *Biochemistry* **30,** 10382–10387.
Vater, W., Fritzsche, W., Schaper, A., Bohm, K. J., Unger, E., and Jovin, T. M. (1995). *J. Cell Sci.* **108,** 1063–1069.
Weisenhorn, A. L., Drake, B., Prater, C. B., Gould, S. A., Hansma, P. K., Ohnesorge, F., Egger, M., Heyn, S. P., and Gaub, H. E. (1990). *Biophys. J.* **58,** 1251–1258.
Yang, J., and Shao, Z. (1995). *Micron* **26,** 35–49.
Yankner, B. A., Dawes, L. R., Fisher, S., Villa-Komaroff, L., Oster-Granite, M. L., and Neve, R. L. (1989). *Science* **245,** 417–420.
Zagorski, M. G., and Barrow, C. J. (1992). *Biochemistry* **31,** 5621–5631.